METALS

Solute segregation and deviation from bulk thermodynamics at nanoscale crystalline defects

Michael S. Titus,[1]* Robert K. Rhein,[1] Peter B. Wells,[1] Philip C. Dodge,[1] Gopal Babu Viswanathan,[2] Michael J. Mills,[2] Anton Van der Ven,[1] Tresa M. Pollock[1]

2016 © The Authors, some rights reserved; exclusive licensee American Association for the Advancement of Science. Distributed under a Creative Commons Attribution NonCommercial License 4.0 (CC BY-NC).

It has long been known that solute segregation at crystalline defects can have profound effects on material properties. Nevertheless, quantifying the extent of solute segregation at nanoscale defects has proven challenging due to experimental limitations. A combined experimental and first-principles approach has been used to study solute segregation at extended intermetallic phases ranging from 4 to 35 atomic layers in thickness. Chemical mapping by both atom probe tomography and high-resolution scanning transmission electron microscopy demonstrates a markedly different composition for the 4–atomic-layer–thick phase, where segregation has occurred, compared to the approximately 35–atomic-layer–thick bulk phase of the same crystal structure. First-principles predictions of bulk free energies in conjunction with direct atomistic simulations of the intermetallic structure and chemistry demonstrate the breakdown of bulk thermodynamics at nanometer dimensions and highlight the importance of symmetry breaking due to the proximity of interfaces in determining equilibrium properties.

INTRODUCTION

In multicomponent crystalline materials, solute segregation at defects, faults, and interfaces has long been considered to have profound effects on material properties. For example, liquid metal embrittlement from Ga or Hg can significantly decrease the elongation to failure due to solute segregation at grain boundaries and cracks in Al alloys (*1*). Hence, liquid metal embrittlement can pose a significant hazard in the aerospace industry, where Al alloys are used extensively. Other material properties thought to be influenced by segregation include grain boundary strength, yield strength, free surface compositions, oxidation, and precipitate growth kinetics (*2*–*4*). A particular subset of crystalline defects includes stacking faults, which are extended two-dimensional crystalline defects. Stacking faults exist in numerous crystalline solids including nanocrystalline metallic alloys, semiconductors, and intermetallic alloys (*5*–*8*).

Solute present in many of these material systems can segregate to or deplete from the stacking faults. This phenomenon was first proposed in 1952 as a way to explain the increases in material strength due to the presence of solute concentrated near the stacking faults across a wide spectrum of metallic alloys (*9*–*14*). Although this phenomenon has been known for nearly seven decades, material design has not yet taken advantage of the effects of solute segregation at stacking faults and other crystalline defects, despite the availability of a full thermodynamic framework for analyzing the driving forces. Because these faults may only be a few atomic layers in thickness, little is known about the changes in the local composition because they thicken to tens of nanometers, transitioning to "bulk" crystalline phases in a thermodynamic sense. Here, we have used two independent experimental techniques to quantitatively examine these nanoscale effects.

A comprehensive understanding of the driving forces behind solute segregation at crystalline defects has eluded researchers due to (i) difficulties in measuring accurate compositions at nanoscale defects, (ii) a lack of accurate thermodynamic properties, and (iii) difficulties in identifying model material systems that inherently aid characterization and simulation of solute segregation. In this contribution, quantitative analysis of segregation at stacking faults was enabled by emerging experimental and first-principles approaches and by examination of a unique material system comprising a solid-solution phase and two intermetallic phases. This particular three-phase material system enables (i) characterization via scanning transmission electron microscopy (STEM) and atom probe tomography (APT) of nanoscale phases (stacking faults) that span large distances, (ii) comparison of the nanoscale stacking fault composition with the corresponding equilibrium bulk phase composition, and (iii) first-principles analysis of the thermodynamic driving forces at finite temperatures, where segregation occurs.

The material system investigated in this contribution incorporates a newly discovered $Co_3(Al,W)$ phase in the Co-Al-W system, whereby γ'-($L1_2$) precipitates are coherently embedded in a γ-(A1) matrix (Fig. 1A) (*15*). The γ crystal structure is face-centered cubic, and the γ' crystal structure is primitive cubic with four atoms per lattice site in an ordered structure (Cu_3Au prototype structure). When Ta is added to the Co-Al-W system, a third phase [Co_3W-($D0_{19}$)] readily forms during high-temperature annealing, with a composition of approximately Co_3W. This phase exhibits an ordered hexagonal close-packed structure. When the Ta-containing single-crystal Co-based alloy is subjected to high-temperature plastic deformation, extended superlattice intrinsic stacking faults (SISFs) form in the γ' precipitates by motion of crystalline defects (dislocations). These SISFs share the same crystal structure as do the equilibrium Co_3W-($D0_{19}$) laths and therefore allow for direct comparisons to be made between the compositions of the nanoscale SISFs and bulk Co_3W phases. Because the material system investigated here is a single crystal that contains no grain boundaries, the nanoscale SISF and the coherently embedded bulk Co_3W phases are present in the same thermodynamic reservoir, having identical chemical potentials and local stress states. Furthermore, the γ', SISF, and Co_3W phases contain about 75 atomic % (at %) Co, which simplifies first-principles modeling because it allows us to approximate the coexisting phases as pseudobinary compounds.

RESULTS

STEM analysis of the postcrept Co-2Ta alloy revealed SISFs on all four {111} planes. The SISFs formed as a result of glide of Shockley

[1]Materials Department, University of California, Santa Barbara, Santa Barbara, CA 93106–5050, USA. [2]Center for Electron Microscopy and Analysis, The Ohio State University, Columbus, OH 43212, USA.
*Corresponding author. Email: titus9@purdue.edu

superpartial dislocations with **b** = $a/3\langle 112\rangle$ (*21*). The superpartial dislocation forms from the reaction of two γ dislocations of type **b** = $a/2\langle 101\rangle$ and $a/2\langle 011\rangle$ (Supplementary Materials). To analyze the solute segregation in the vicinity of these SISFs and their local structure, we extracted TEM specimens from the bulk material by use of a focused ion beam and scanning electron microscope (FIB-SEM) such that the specimen normal was approximately parallel to the [110] direction. An overview of the region of interest for the alloy is shown in Fig. 1B, and a schematic of the shearing process responsible for SISF formation is shown in Fig. 1C.

High-resolution STEM high-angle annular dark-field (HAADF) imaging revealed a Co_3W-($D0_{19}$) lath coherently embedded within a region of γ′ phase, as shown in Figs. 1B and 2A. A SISF within the γ′ phase was located parallel to the lath, as shown in Fig. 2A. Fourier transforms of the atomic-resolution STEM images revealed superlattice reflections that were consistent with a $D0_{19}$ structure for both the Co_3W lath and the SISF.

Vertically integrated energy-dispersive x-ray spectroscopy (EDS) line scans across the image in Fig. 2A revealed a simultaneous enhancement in W and Ta content and a decrease in Co and Al content near the lath and fault, as shown in Fig. 2A. This result is further corroborated by the vertically integrated line scans of the HAADF image, which also revealed an increase in image intensity for both the Co_3W lath and SISF relative to the γ′ phase, as shown in fig. S1. This is expected due to the semiquantitative nature of the HAADF image, where the image intensity scales as the average Z to the 1.7 to 2 power (*22*).

APT was also carried out to provide complementary evidence of segregation at SISFs. Approximately [111]-oriented APT needles were machined using a FIB-SEM (Supplementary Materials).

Clear evidence of Al depletion at planar phases was readily observed in the reconstructed Al atom map (shown in Fig. 2B), but only slight variations in Co, W, and Ta were readily observed from the atom maps. One-dimensional line profiles across the normal of the planar phases revealed segregation of W and Ta and a depletion of Co and Al, as shown in Fig. 2B. The profile used a fixed bin width of 0.15 nm, and the moving average of two consecutive bins was used to reduce data scatter for visual clarity. This moving average did not alter the total integrated excess W + Ta signal across the fault by more than 1%. The observed segregation behavior (composition and size) at the two bordering phases determined from APT is in agreement with the result from the high-resolution STEM EDS analysis of the SISF, in which the maximum W + Ta composition was found to be 18.9 and 21 at % for STEM EDS and APT analyses, respectively.

Quantitative TEM EDS composition analysis can be influenced by thermally scattered electrons whose anomalous contributions to the EDS signal depend on the atomic species present, specimen thickness, and crystal orientation (*23*, *24*). Because of these effects, the signal is undoubtedly delocalized, as shown by the broad W + Ta peak around the SISF in Fig. 2A. However, additional analysis that includes beam delocalization revealed only a small (<0.6 at %) increase of the solute concentration to 19.5 at % within the SISF relative to the initial analysis, as shown in fig. S2. Unfortunately, current quantitative TEM EDS work has focused mostly on oxide materials including $SrTiO_3$, and it remains to be seen how delocalization affects the EDS signal in metallic specimens. Similar issues may exist in APT analysis, as noted in the Supplementary Materials. However, simulations have shown that although these artifacts may result in an incorrect measurement of the thickness of the SISF, it should not significantly degrade composition measurements (*25*). Although full simulations of both the TEM and APT analyses are required for rigorous composition analysis, the results shown here demonstrate a size dependence on the equilibrium composition within the faults and nanophases.

Without the high-resolution STEM information on local structure, these defects in the APT specimen could not be rigorously determined. Furthermore, the middle planar phase in the APT reconstruction exhibited segregation behavior similar to that of the Co_3W lath from the STEM EDS analysis, but the thickness of the middle APT phase was significantly smaller than that of the Co_3W lath from the STEM EDS data set. It is unclear whether this phase is a thin Co_3W lath or a superlattice extrinsic stacking fault consisting of five atomic layers of $D0_{24}$ structure, which has been shown to exhibit similar segregation

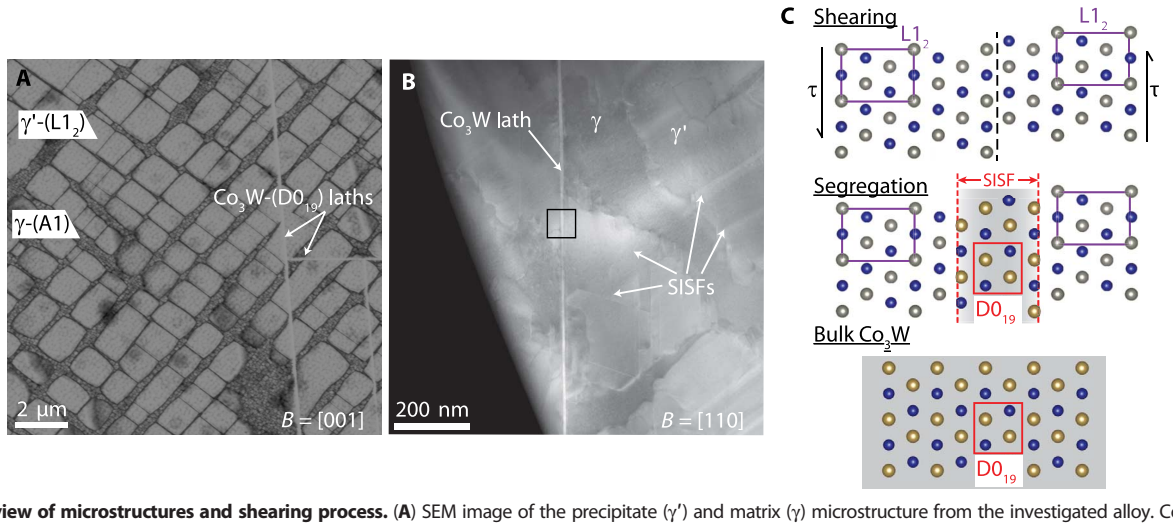

Fig. 1. Overview of microstructures and shearing process. (**A**) SEM image of the precipitate (γ′) and matrix (γ) microstructure from the investigated alloy. Co_3W laths are observed near the right of the image. (**B**) STEM image of the deformed Co-2Ta microstructure. A Co_3W lath was observed to cross a γ′ precipitate. Numerous SISFs were observed to cross through the γ′ precipitates. (**C**) Schematic of the shearing sequence that is required to form SISFs in the γ′-($L1_2$) blocks. The γ′-($L1_2$) blocks must first shear, and segregation at the newly created SISF may occur, which enables the local SISF-($D0_{19}$) composition to become more like the bulk Co_3W-($D0_{19}$) composition. Molecular drawings completed in VESTA (*48*).

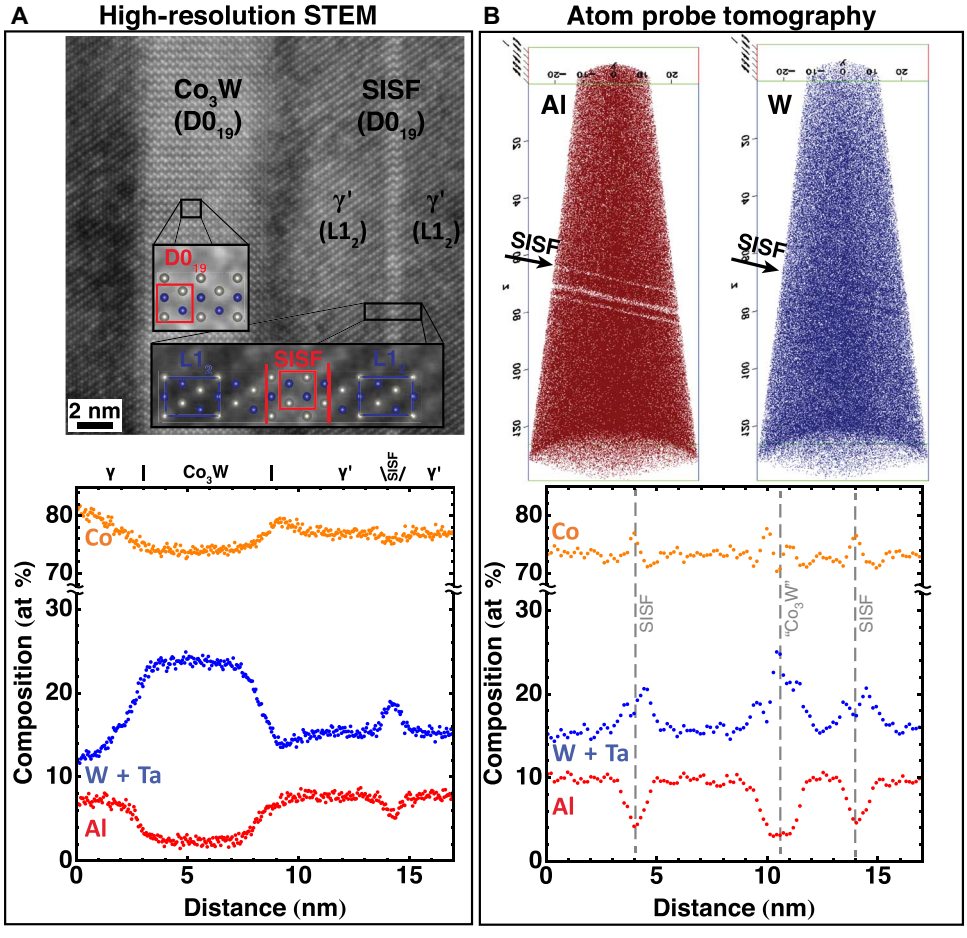

Fig. 2. Composition analysis at the stacking fault. (**A**) High-resolution STEM HAADF image from the area denoted by the black box from Fig. 1B. A SISF is located adjacent to a Co_3W lath. The vertically integrated EDS line scan across the STEM HAADF reveals differences in the local composition of the Co_3W lath and the SISF. (**B**) The high-resolution STEM EDS data are in agreement with APT reconstructions, where a SISF intersects the APT tip on a {111} plane. Al atoms (50%) and W atoms (20%) are shown for clarity.

characteristics to the SISFs (*26*). The mismatch between the compositions at the SISFs and the Co_3W-like phase from the APT results reveals that, despite exhibiting identical crystal structures, the equilibrium concentration of solute at the SISFs is significantly less than the concentration of W and Ta in the thermodynamically equilibrated Co_3W-($D0_{19}$) phase. Differences in composition between the two phases cannot be due to the differences in the chemical reservoir because the local stress state and thermodynamic boundary conditions are identical between the two phases. Furthermore, the agreement between the STEM and APT chemical profiles suggests that the measured segregation profiles are not strongly influenced by any artifacts of the techniques, as discussed above.

Currently, it is unknown whether the equilibrium concentration of the SISF can be predicted. Predicting the equilibrium composition at the SISF would enable predictions to be made of the planar defect energy of the SISF. Previous research revealed that segregation of W and Ta to SISFs significantly decreases the SISF energy (*26*). This reduction, in turn, decreases the shear stress required for γ′ precipitate shearing and affects the high-temperature strength by enabling γ′ shearing at elevated temperatures (*26*). Thus, predicting the equilibrium SISF composition will aid in predicting the mechanical properties of these alloys. Analysis of the local composition of the SISF will now be made in the context of current thermodynamic models for nanoscale phases.

First-principles modeling

Multiphase equilibrium is determined by the equality of the chemical potentials of the mobile species. This equilibrium criterion in alloys is equivalent to the well-known common tangent construction in which the (hyper) plane that is simultaneously tangent to the free energies of the coexisting phases determines their equilibrium atomic fractions. In contrast, segregation at stacking faults is dictated by the Suzuki criterion, which requires an equality of chemical potential differences. This equilibrium criterion arises from the constraint that segregation occurs at the expense of other atoms at the stacking fault while keeping the size of the stacking fault fixed. Because the Co concentration within the γ′ and Co_3W phases remains close to 75 at %, we can analyze the various equilibrium criteria along a pseudobinary Co_3Al-Co_3W composition axis. The Suzuki segregation criterion then reduces to

$$\left(\frac{\partial g^{\gamma'}\left(c_W^{\chi}\right)}{\partial c_W^{\chi}}\right)\bigg|_{c_{\gamma'},N} = \left(\frac{\partial g^{\chi}\left(c_W^{\chi}\right)}{\partial c_W^{\chi}}\right)\bigg|_{c_{\chi},N} \quad (1)$$

where g^i is the Gibbs free energy per atom of the γ′ and χ-(SISF/Co_3W) phases, c_W^i is the W concentration in the γ′ or χ-(SISF/Co_3W) phase, and c_i is the equilibrium composition of the γ′ or χ phase. Because both the SISF and Co_3W phases exhibit an identical crystal structure ($D0_{19}$), a common approximation in the application of the Suzuki criterion is to use the bulk free energy to predict segregation at the stacking fault (see the Supplementary Materials and Eq. 1). The derivatives are taken, keeping the Co concentration constant. Thus, for a known composition of γ′, the slope of the Gibbs free energy curve (or equivalently, exchange potential) may be determined and matched to the equivalent slope on the χ-(SISF/Co_3W) phase Gibbs free energy curve, which is located at the SISF equilibrium composition.

We calculated the bulk free energies of $L1_2$ and $D0_{19}$ along the pseudobinary Co_3Al-Co_3W composition axis by combining a first-principles parameterized cluster expansion with grand canonical Monte Carlo simulations (see the Supplementary Materials and figs. S3 and S4 for more information). Contributions to the free energy from vibrational excitations were calculated within the quasi-harmonic approximation, as described by Rhein *et al.* (*27*). First-principles density functional theory calculations were performed with VASP (see the Supplementary Materials) (*28*–*32*), whereas the construction of the cluster expansion, the Monte Carlo simulations, and the phonon calculations were performed with CASM (see the Supplementary Materials) (*33*–*36*).

Figure 3A shows the calculated free energies of the $L1_2$ and $D0_{19}$ phases at 900°C (the experimental test temperature). The $L1_2$ phase exhibits a tendency for W and Al to form a solid solution over the minority $L1_2$ sublattice along the Co_3Al-Co_3W pseudobinary composition axis, whereas $D0_{19}$ is predicted to phase-separate along the same pseudobinary. At low Al compositions, $L1_2$ has a lower free energy than $D0_{19}$, but it is not globally stable and is predicted to decompose into a Co-rich phase and a B2 CoAl compound (*27*). However, for W-rich concentrations, Fig. 3A suggests that a two-phase region should exist between the $L1_2$ and $D0_{19}$ phases, as determined by the common tangent construction along the pseudobinary composition axis. The common tangent construction predicts that the composition of $D0_{19}$, when in equilibrium with $L1_2$, should be close to that of stoichiometric Co_3W, having a negligible Al concentration. This prediction is consistent with the experimental composition in the 35–atomic-layer–thick $D0_{19}$ laths coherently embedded within $L1_2$ (Fig. 2A), suggesting that bulk thermodynamics remains accurate even for thin laths that are 35 atomic layers thick.

Application of the Suzuki criterion using bulk free energies to estimate the concentration along the SISF leads to a concentration that is very similar to that obtained with the common tangent construction. This is shown graphically in Fig. 3B, where a tangent to the free energy of $D0_{19}$ has the same slope as the tangent to $L1_2$ at its experimental bulk concentration of $Co_{0.75}Al_{0.11}W_{0.14}$. The predicted Suzuki concentration in the SISF when using the bulk free energy for $D0_{19}$ is close to 24 at %, a value that is substantially higher than that observed experimentally in the SISF. This shows a clear breakdown of bulk thermodynamics for SISFs and, by extension, for phases that are only a few atomic layers thick.

To account for the broken symmetries due to the nanoscale thickness of the SISF, we explicitly performed a statistical mechanics study of a periodic 32-atom $L1_2$ supercell containing a SISF, as shown in Fig. 4A. A cluster expansion Hamiltonian was parameterized from first principles for all the non-Co sites of the supercell and subjected to Monte Carlo simulations to predict the equilibrium concentrations along a SISF embedded within an $L1_2$ phase.

Figure 4B shows the calculated sublattice site composition of the SISF as a function of the average $L1_2$ composition at 900°C. As shown by the dashed lines in Fig. 4B, an average $L1_2$ composition of $Co_{0.75}Al_{0.11}W_{0.14}$ will be accompanied by an average composition in the SISF that is predicted to be 21 at % W. This value is smaller than that predicted using the bulk free energy for $D0_{19}$ to approximate the thermodynamic properties of the SISF, and it is in agreement with the experimentally measured segregation concentration along the SISF.

DISCUSSION

It has long been known that the thermodynamic properties of a material can change markedly as it is scaled to nanometer dimensions. Nevertheless, quantifying these changes experimentally has proved challenging due to difficulties in controlling particle shape and size as well as thermal and chemical reservoirs that impose thermodynamic boundary conditions. A unique, coherent, multiphase equilibrium in the Co-Al-W ternary (with dilute Ta additions) has allowed us

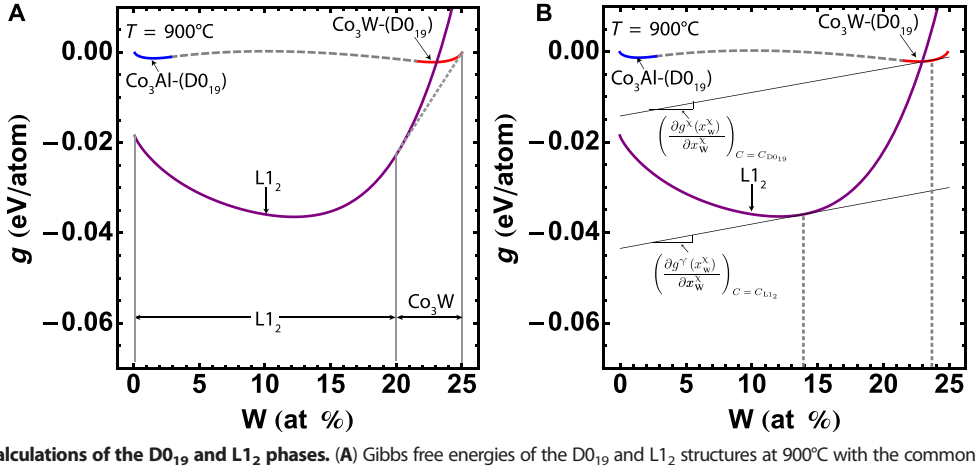

Fig. 3. First-principles calculations of the $D0_{19}$ and $L1_2$ phases. (**A**) Gibbs free energies of the $D0_{19}$ and $L1_2$ structures at 900°C with the common tangent construction. The $L1_2$ structure is predicted to be stable from 0 to 20 at % W, and the Co_3W phase is predicted to be stable from 20 to 25 at % W. (**B**) Gibbs free energies of the $D0_{19}$ and $L1_2$ structures at 900°C with the Suzuki segregation criterion from Eq. 1 satisfied. It is represented by the two compositions: c_{L12} = Co-11Al-14W (at %) and c_{D019} = Co-1Al-24W (at %).

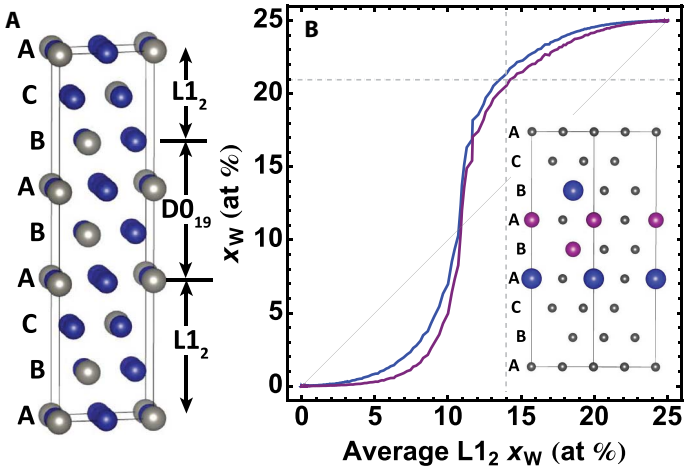

Fig. 4. Direct atomistic simulation of the equilibrium stacking fault composition. (**A**) $L1_2 + D0_{19}$ supercell (*48*). (**B**) (Inset) Average concentration for each sublattice site (colored) as a function of the average $L1_2$ composition determined from the $L1_2$ layers in the 32-atom supercell. For W-rich $L1_2$ compositions, the average composition within the SISF is higher, as shown by the dashed gray lines located at the γ′ composition of Co-11Al-14W (at %).

to create highly idealized $D0_{19}$ plate–like precipitates that have thicknesses that range from 4 to 35 atomic layers, which are coherently embedded within $L1_2$ precipitates. The thicker $D0_{19}$ plates emerged through decomposition reactions, whereas the 4–atomic-layer–thick plates of $D0_{19}$ were generated through plastic deformation that causes shearing of the $L1_2$ intermetallic phase. This shearing creates SISFs that are less than a nanometer thick but thousands of atomic layers in length.

The SISFs form in the vicinity of and parallel to the thicker $D0_{19}$ plates, ensuring not only that the different precipitates reside in an identical chemical reservoir but also that they have very similar mechanical boundary conditions. Using emerging imaging and spectroscopy approaches complemented with first-principles computations, we could quantitatively assess the thermodynamic driving forces and changes in the degree of segregation as a function of size. The experimental and theoretical results above conclusively demonstrate that (i) the equilibrium composition of SISFs in a γ′-($L1_2$) precipitate is not equal to the equilibrium composition of the bulk Co_3W phase of the same crystal structure and (ii) the equilibrium composition of the SISF is more accurately predicted using direct, atomistic simulations of a SISF embedded in a host γ′ matrix as opposed to using bulk free energy descriptions in the context of the Suzuki equilibrium criterion.

The difference in equilibrium compositions between the SISF and the thicker plates of Co_3W-($D0_{19}$) is perhaps not surprising when considering that the SISF is only 4 atomic layers thick and is not a bulk phase. The finite thickness of the SISF means that interactions between second nearest neighbors (on the Al and W sublattice) located in the SISF and adjacent $L1_2$ matrix are possible. This is corroborated by inspection of the clusters incorporated in the cluster expansion for the $L1_2 + D0_{19}$ supercell, whereby 3 of the 11 multiplet clusters contain interactions between the $D0_{19}$ and $L1_2$ portions of the supercell—interactions that are not present in either of the bulk phase cluster expansions. In this context, it is possible to rationalize the lower W concentration within the SISF (that is, the 4–atomic-layer–thick $D0_{19}$ phase) as compared to that in the 35–atomic-layer–thick $D0_{19}$ lath by inspection of the bulk free energies of $L1_2$ and $D0_{19}$. Because atoms within the SISF sample not only the hexagonal close-packed environment of the $D0_{19}$ structure but also the cubic environment of $L1_2$ through second nearest-neighbor interactions, the W concentration in the SISF is a compromise between the high value of bulk $D0_{19}$ and the lower value of bulk $L1_2$.

Despite the difference in compositions between the SISF and bulk $D0_{19}$ phases, segregation of W and Ta even in small concentrations significantly reduces the SISF energy inside the γ′ phase (*26*). The reduction in SISF energy assists the dislocation shearing process, whereby the critical stress for γ′ shearing is well known to decrease linearly with decreasing SISF or, more generally, planar defect energy (*37*). Compression tests conducted at 900°C at a strain rate of 10^{-4} s^{-1} revealed segregation at SISFs, as shown in fig. S5. Therefore, we believe that the process of segregation occurs quickly over these small length scales at elevated temperatures. This suggests that the diffusion of elements near SISFs is not the rate-limiting step for plastic deformation, but instead, the SISF energy quickly decreases and therefore enables the leading dislocation to shear the γ′ phase under a lower applied stress.

The decrease in the stress required for γ′ shearing is not necessarily detrimental to high-temperature creep strength because the formation of very stable coherent boundaries, such as the SISFs investigated here, have been shown to provide strength benefits in other material systems (*38*). Hence, segregation at SISFs serves to increase the susceptibility of SISF formation and therefore likely increases the strength of the alloys during high-temperature creep by the aforementioned mechanism.

CONCLUSIONS

High-resolution STEM HAADF imaging, EDS mapping, and APT revealed solute segregation in the vicinity of plasticity-induced SISFs. Solute segregation at SISFs was consistent with a change in composition from the host γ′ phase toward the thermodynamically stable Co_3W bulk phase. However, the equilibrium composition of the nanoscaled SISFs was not observed to be identical to that of the bulk Co_3W phase, despite the two phases exhibiting identical crystal structures. First-principles calculations incorporating ground-state formation energies, Monte Carlo simulations, and temperature-dependent phonon energetics using bulk free energies (Eq. 1) qualitatively predict a change in composition toward the bulk Co_3W phase but fail to reproduce experimental observations quantitatively. Instead, a statistical mechanics treatment of an explicit SISF coherently embedded in an $L1_2$ matrix predicted segregation tendencies in better conformity with experiment. These high-resolution imaging, spectroscopy, and tomography experiments coupled with first-principles simulations conclusively demonstrate a breakdown of bulk thermodynamics at the nanoscale level despite the presence of an identical chemical reservoir surrounding both the nanoscale and bulk phases in question.

MATERIALS AND METHODS

A single-crystal composition of Co-8.8Al-9.8W-2.0Ta (at %) was grown via the single-crystal Bridgman process. This alloy design builds on a model Co-Al-W ternary alloy whose composition has been previously shown to exhibit both the γ and γ′ phases (*15*). After crystal growth, subsequent material heat treatments yielded the structure shown in Fig. 1A. In addition to the γ matrix and γ′ precipitates, there

was a small volume fraction of the Co_3W-($D0_{19}$) phase, which is in equilibrium with the γ′ phase at elevated temperatures (*16*).

To form nanoscale SISFs within the γ′ blocks, the material was plastically deformed under tension at 900°C (Supplementary Materials). The deformed structure was investigated using high-resolution STEM on an FEI Titan STEM equipped with a Super-X EDS system, which consisted of four radially positioned silicon drift detectors. This system was used for EDS mapping of nanoscale defects and is described in further detail in previous works (*17–19*). The EDS signal was quantified using the built-in Cliff-Lorimer TEM analysis housed in the ESPRIT software. Additional nanoscale composition analysis was conducted by APT (Supplementary Materials) (*20*). APT was carried out in voltage evaporation mode using Cameca 3000X at a voltage pulse amplitude of 20% of the standing dc voltage, a target evaporation rate of 0.40%, and a temperature of approximately 50 K. The APT experiment and reconstruction are further described in detail in the Supplementary Materials.

SUPPLEMENTARY MATERIALS

Supplementary material for this article is available at http://advances.sciencemag.org/cgi/content/full/2/12/e1601796/DC1

Supplementary Materials and Methods

Supplementary Text

table S1. Compositions and heat treatment conditions.

table S2. Creep testing conditions.

fig. S1. HAADF STEM intensity profile.

fig. S2. Gaussian distribution fit and model of the W + Ta composition at the SISF.

fig. S3. Calculated and predicted ground-state energies for structures used in the cluster expansion.

fig. S4. Effective cluster interaction parameters used in the cluster expansion.

fig. S5. HAADF STEM image of specimen tested at a strain rate of 10^{-4} s^{-1}.

References (*39–47*)

REFERENCES AND NOTES

1. M. G. Nicholas, C. F. Old, Liquid metal embrittlement. *J. Mater. Sci.* **14**, 1–18 (1979).
2. A. Cottrell, Effect of solute atoms on the behaviour of dislocations, in *Report on Conference of the Strength of Solids* (Physical Society, 1948), pp. 30–37.
3. C. T. Liu, C. L. White, J. A. Horton, Effect of boron on grain-boundaries in Ni_3Al. *Acta Metall.* **33**, 213–229 (1985).
4. A. G. Evans, J. W. Hutchinson, Y. Wei, Interface adhesion: Effects of plasticity and segregation. *Acta Mater.* **47**, 4093–4113 (1999).
5. D. Shechtman, M. J. Blackburn, H. A. Lipsitt, The plastic deformation of TiAl. *Metall. Trans.* **5**, 1373–1381 (1974).
6. L. Lu, Y. Shen, X. Chen, L. Qian, K. Lu, Ultrahigh strength and high electrical conductivity in copper. *Science* **304**, 422–426 (2004).
7. R. Liu, A. Bell, F. A. Ponce, C. Q. Chen, J. W. Yang, M. A. Khan, Luminescence from stacking faults in gallium nitride. *Appl. Phys. Lett.* **86**, 021908 (2005).
8. J. F. Nie, Y. M. Zhu, J. Z. Liu, X. Y. Fang, Periodic segregation of solute atoms in fully coherent twin boundaries. *Science* **340**, 957–960 (2013).
9. H. Suzuki, Chemical interaction of solute atoms with dislocations. *Sci. Rep. Res. Inst. Tohoku Univ.* **A4**, 455–463 (1952).
10. H. Suzuki, The yield strength of binary alloys, in *Dislocations and Mechanical Properties of Crystals* (John Wiley, 1957), pp. 361–390.
11. H. Suzuki, Segregation of solute atoms to stacking faults. *J. Phys. Soc. Jpn.* **17**, 322–325 (1962).
12. G. W. Han, I. P. Jones, R. E. Smallman, Direct evidence for Suzuki segregation and Cottrell pinning in MP159 superalloy obtained by FEG(S)TEM/EDX. *Acta Mater.* **51**, 2731–2742 (2003).
13. Y. Koizumi, T. Nukaya, S. Suzuki, S. Kurosu, Y. Li, H. Matsumoto, K. Sato, Y. Tanaka, A. Chiba, Suzuki segregation in Co–Ni-based superalloy at 973K: An experimental and computational study by phase-field simulation. *Acta Mater.* **60**, 2901–2915 (2012).
14. S. Y. Yang, M. Jiang, L. Wang, Thermodynamic description of the γ′ phase in the Co-Al-W based superalloys. *Mater. Sci. Forum* **747–748**, 654–658 (2013).
15. J. Sato, T. Omori, K. Oikawa, I. Ohnuma, R. Kainuma, K. Ishida, Cobalt-base high-temperature alloys. *Science* **312**, 90–91 (2006).
16. J. Zhu, M. S. Titus, T. M. Pollock, Experimental investigation and thermodynamic modeling of the co-rich region in the Co-Al-Ni-W quaternary system. *J. Phase Equilib. Diff.* **35**, 595–611 (2014).
17. A. J. D'Alfonso, B. Freitag, D. Klenov, L. J. Allen, Atomic-resolution chemical mapping using energy-dispersive x-ray spectroscopy. *Phys. Rev. B* **81**, 100101(R) (2010).
18. M.-W. Chu, S. C. Liou, C.-P. Chang, F.-S. Choa, C. H. Chen, Emergent chemical mapping at atomic-column resolution by energy-dispersive X-ray spectroscopy in an aberration-corrected electron microscope. *Phys. Rev. Lett.* **104**, 196101 (2010).
19. L. J. Allen, A. J. D'Alfonso, B. Freitag, D. O. Klenov, Chemical mapping at atomic resolution using energy-dispersive x-ray spectroscopy. *MRS Bull.* **37**, 47–52 (2012).
20. M. S. Titus, A. Suzuki, T. M. Pollock, High temperature creep of new $L1_2$-containing cobalt-base superalloys, in *Superalloys 2012* (John Wiley & Sons Inc., 2012), pp. 823–832.
21. A. Suzuki, T. M. Pollock, High-temperature strength and deformation of γ-γ′ two-phase Co–Al–W-base alloys. *Acta Mater.* **56**, 1288–1297 (2008).
22. S. J. Pennycook, Z-contrast stem for materials science. *Ultramicroscopy* **30**, 58–69 (1989).
23. B. D. Forbes, A. J. D'Alfonso, R. E. A. Williams, R. Srinivasan, H. L. Fraser, D. W. McComb, B. Freitag, D. O. Klenov, L. J. Allen, Contribution of thermally scattered electrons to atomic resolution elemental maps. *Phys. Rev. B* **86**, 024108 (2012).
24. Z. Chen, M. Weland, X. Sang, W. Xu, J. H. Dycus, J. M. LeBeau, A. J. D'Alfonso, L. J. Allen, S. D. Findlay, Quantitative atomic resolution elemental mapping via absolute-scale energy dispersive X-ray spectroscopy. *Ultramicroscopy* **168**, 7–16 (2016).
25. F. Vurpillot, D. Larson, A. Cerezo, Improvement of multilayer analyses with a three-dimensional atom probe. *Surf. Interface Anal.* **36**, 552–558 (2004).
26. M. S. Titus, A. Mottura, G. B. Viswanathan, A. Suzuki, M. J. Mills, T. M. Pollock, High resolution energy dispersive spectroscopy mapping of planar defects in $L1_2$-containing Co-base superalloys. *Acta Mater.* **89**, 423–437 (2015).
27. R. K. Rhein, P. C. Dodge, M.-H. Chen, M. S. Titus, T. M. Pollock, A. Van der Ven, Role of vibrational and configurational excitations in stabilizing the $L1_2$ structure in Co-rich Co-Al-W alloys. *Phys. Rev. B* **92**, 174117 (2015).
28. G. Kresse, J. Furthmüller, Efficient iterative schemes for ab initio total-energy calculations using a plane-wave basis set. *Phys. Rev. B* **54**, 11169–11186 (1996).
29. J. Hafner, Materials simulations using VASP—A quantum perspective to materials science. *Comput. Phys. Commun.* **177**, 6–13 (2007).
30. P. E. Blöchl, Projector augmented-wave method. *Phys. Rev. B* **50**, 17953–17979 (1994).
31. G. Kresse, D. Joubert, From ultrasoft pseudopotentials to the projector augmented-wave method. *Phys. Rev. B* **59**, 1758–1775 (1999).
32. J. P. Perdew, K. Burke, M. Ernzerhof, Generalized gradient approximation made simple. *Phys. Rev. Lett.* **77**, 3865–3868 (1996).
33. A. Van der Ven, J. C. Thomas, Q. Xu, J. Bhattacharya, Linking the electronic structure of solids to their thermodynamic and kinetic properties. *Math. Comput. Simul.* **80**, 1393–1410 (2010).
34. J. C. Thomas, A. Van der Ven, Finite-temperature properties of strongly anharmonic and mechanically unstable crystal phases from first principles. *Phys. Rev. B* **88**, 214111 (2013).
35. B. Puchala, A. Van der Ven, Thermodynamics of the Zr-O system from first-principles calculations. *Phys. Rev. B* **88**, 094108 (2013).
36. CASM, v0.1.0 (2015); https://github.com/prisms-center/CASMcode.
37. J. P. Hirth, Thermodynamics of stacking faults. *Metall. Trans.* **1**, 2367–2374 (1970).
38. K. Lu, L. Lu, S. Suresh, Strengthening materials by engineering coherent internal boundaries at the nanoscale. *Science* **324**, 349–352 (2009).
39. H. J. Monkhorst, J. D. Pack, Special points for Brillouin-zone integrations. *Phys. Rev. B* **13**, 5188–5192 (1976).
40. A. Van der Ven, J. C. Thomas, Q. Xu, B. Swoboda, D. Morgan, Nondilute diffusion from first principles: Li diffusion in Li_xTiS_2. *Phys. Rev. B* **78**, 104306 (2008).
41. J. M. Sanchez, J. D. Becker, The role of the cluster variation method in the first principles calculation of phase diagrams. *Prog. Theor. Phys. Suppl.* **115**, 131–145 (1994).
42. G. L. W. Hart, V. Blum, M. J. Walorski, A. Zunger, Evolutionary approach for determining first-principles hamiltonians. *Nat. Mater.* **4**, 391–394 (2005).
43. A. van de Walle, G. Ceder, Automating first-principles phase diagram calculations. *J. Phase Equilib.* **23**, 348–359 (2002).
44. N. W. Ashcroft, N. D. Mermin, *Solid State Physics* (Cengage Learning, ed. 1, 1976).
45. S. Wei, M. Y. Chou, Ab initio calculation of force constants and full phonon dispersions. *Phys. Rev. Lett.* **69**, 2799–2802 (1992).
46. A. van de Walle, G. Ceder, The effect of lattice vibrations on substitutional alloy thermodynamics. *Rev. Mod. Phys.* **74**, 11–45 (2002).
47. W. W. Xu, J. J. Han, Z. W. Wang, C. P. Wang, Y. H. Wen, X. J. Liua, Z. Z. Zhu, Thermodynamic, structural and elastic properties of Co_3X (X = Ti, Ta, W, V, Al) compounds from first-principles calculations. *Intermetallics* **32**, 303–311 (2013).
48. K. Momma, F. Izumi, *VESTA 3* for three-dimensional visualization of crystal, volumetric and morphology data. *J. Appl. Crystallogr.* **44**, 1272–1276 (2011).

Acknowledgments: We would like to thank C. Dreyer and A. Natarajan (University of California, Santa Barbara) for useful discussion regarding density functional theory and Monte Carlo methods. We would also like to thank I. Chen (University of California, Santa Barbara) for input regarding vibrational free energy calculations. Furthermore, we would like to

acknowledge insightful discussions with A. Mottura (University of Birmingham) regarding first-principles calculations. **Funding:** This work was supported by the NSF Designing Materials to Revolutionize and Engineer our Future grant DMR 1534264. We acknowledge support from the Center for Scientific Computing at the California NanoSystems Institute and Materials Research Laboratory (MRL): NSF Materials Research Science and Engineering Center (MRSEC) (DMR-1121053) and NSF CNS-0960316. The MRL Shared Experimental Facilities are supported by the MRSEC Program of the NSF under award no. DMR-1121053, a member of the NSF-funded Materials Research Facilities Network (www.mrfn.org). **Author contributions:** M.S.T. and G.B.V. conducted the TEM analysis. Additionally, M.J.M. and T.M.P. assisted with the interpretation of the TEM results. M.S.T., R.K.R., P.C.D., and A.V.d.V. calculated the Gibbs free energies and equilibrium compositions for the $D0_{19}$ and $L1_2$ phases. P.B.W. conducted the APT experiments and analysis. M.J.M., A.V.d.V., and T.M.P. supervised the study, especially relating to TEM, first-principles calculations, and material testing and characterization, respectively. All authors extensively discussed the results, first-principles calculations, and thermodynamics models and contributed to the writing of this manuscript. **Competing interests:** The authors declare that they have no competing interests. **Data and materials availability:** All data needed to evaluate the conclusions in the paper are present in the paper and/or the Supplementary Materials. Additional data related to this paper may be requested from the authors.

Submitted 3 August 2016
Accepted 18 November 2016
Published 21 December 2016
10.1126/sciadv.1601796

Citation: M. S. Titus, R. K. Rhein, P. B. Wells, P. C. Dodge, G. B. Viswanathan, M. J. Mills, A. Van der Ven, T. M. Pollock, Solute segregation and deviation from bulk thermodynamics at nanoscale crystalline defects. *Sci. Adv.* **2**, e1601796 (2016).